

# Layered nano-mosaic of niobium disulfide heterostructures by direct sulfidation of niobium carbides MXenes for hydrogen evolution

*Samantha Husmann,<sup>1</sup> Mohammad Torkamanzadeh,<sup>1,2</sup> Kun Liang,<sup>3</sup>*

*Ahmad Majed,<sup>3</sup> Chaochao Dun,<sup>4</sup> Jeffrey J Urban,<sup>4</sup> Michael Naguib<sup>3,\*</sup> Volker Presser,<sup>1,2,5,\*</sup>*

<sup>1</sup> *INM - Leibniz Institute for New Materials, D2 2, 66123, Saarbrücken, Germany*

<sup>2</sup> *Department of Materials Science & Engineering, Saarland University, Campus D2 2, 66123, Saarbrücken, Germany*

<sup>3</sup> *Department of Physics and Engineering Physics, Tulane University, New Orleans, Louisiana 70118, United States of America*

<sup>4</sup> *The Molecular Foundry, Lawrence Berkeley National Laboratory, Berkeley, California 94720, United States of America*

<sup>5</sup> *Saarene, Saarland Center for Energy Materials and Sustainability, Campus C4 2, 66123 Saarbrücken, Germany*

\* Corresponding authors' email: [naguib@tulane.edu](mailto:naguib@tulane.edu) (MN), [volker.presser@leibniz-inm.de](mailto:volker.presser@leibniz-inm.de) (VP)

## Abstract

MXene-transition metal dichalcogenides (TMD) heterostructures are synthesized through one-step heat treatment of Nb<sub>2</sub>C and Nb<sub>4</sub>C<sub>3</sub>. These MXenes were used without delamination or any pre-treatment. Heat treatments accomplish the sacrificial transformation of these MXenes into TMD (NbS<sub>2</sub>) at 700 °C and 900 °C under H<sub>2</sub>S. The role of starting MXene phase in the derivative morphology is exhibited for the first time. It is shown that while treatment of Nb<sub>2</sub>C at 700 °C leads to the formation of pillar-like structures on parent MXene, Nb<sub>4</sub>C<sub>3</sub> produces nano-mosaic layered NbS<sub>2</sub>. At 900 °C, both MXene phases fully convert into nano-mosaic layered NbS<sub>2</sub> preserving parent MXene's layered morphology. When tested as electrodes for hydrogen evolution reaction, Nb<sub>4</sub>C<sub>3</sub> derived hybrids showed better performance than Nb<sub>2</sub>C derivatives. The Nb<sub>4</sub>C<sub>3</sub>-derived heterostructure exhibited a low overpotential of 198 mV at 10 mA cm<sup>-2</sup>, and a Tafel slope of 122 mV dec<sup>-1</sup>, with good cycling stability in an acidic electrolyte.

## Keywords

carbides; catalysis; hydrogen evolution reaction; metal sulfides; MXenes

## 1. Introduction

MAX phases, such as  $\text{Ti}_3\text{AlC}_2$ , are nanolamellar structures generally comprised of an early transition metal element (M), a group 13-15 element (A), and carbon and/or nitrogen (X) with a composition of  $\text{M}_{n+1}\text{AX}_n$  where n can be 1-4.<sup>[1]</sup> As the metallic bond between M-A is weaker than the mixed metallic-covalent bond between M-X, elements at the A-site (e.g., Al) can be selectively removed to result in layered MX structures (e.g.,  $\text{Ti}_3\text{C}_2$ ),<sup>[2]</sup> named MXenes.<sup>[3]</sup> The typical HF acid etching in an aqueous environment converts MAX into MXene while rendering MXene surfaces terminated with -O, -OH, and -F functionalities.<sup>[4]</sup> Since their discovery in 2011,<sup>[2]</sup> MXene has so far found a plethora of wide-ranging applications such as in energy storage devices,<sup>[5]</sup> electrocatalysis,<sup>[6, 7]</sup> sensing,<sup>[8]</sup> and environmental remediation.<sup>[9]</sup> Each of these applications capitalizes on a specific combination of unique properties offered by MXenes: a layered 2D structure that can accommodate ions,<sup>[10]</sup> an excellent electrical conductivity (a conductivity up to  $24 \cdot 10^3 \text{ S cm}^{-1}$  was measured for  $\text{Ti}_3\text{C}_2$ ),<sup>[11]</sup> a hydrophilic nature (depending on the surface terminations),<sup>[3]</sup> and rich electrochemically active sites,<sup>[7]</sup> among others.

Shortly after their discovery, research efforts have been made to modify MXenes further to improve their performances.<sup>[12]</sup> For instance, alternative etching methods,<sup>[13]</sup> such as HCl/LiF mixtures,<sup>[14]</sup>  $\text{NH}_4\text{HF}_2$ ,<sup>[15]</sup> molten salt etching,<sup>[16]</sup> and alkali etching<sup>[17]</sup> have been proposed to favorably alter the surface terminations,<sup>[14]</sup> interlayer spacings,<sup>[18]</sup> electronic,<sup>[19]</sup> and electrochemical<sup>[20]</sup> properties of MXene. In contrast to techniques such as layer-by-layer self-assembly<sup>[21]</sup> or pillaring<sup>[20, 22]</sup> of the MXene sheets where organic molecules need to be present during synthesis, one-step modification methods often offer simplicity and more significant potential for industrial-scale applications. The first report on the latter approach was the one-step conversion of  $\text{Ti}_3\text{C}_2$  into  $\text{TiO}_2\text{-C}$  hybrids by oxidation of the MXene precursors in air,  $\text{CO}_2$ , or hydrothermally.<sup>[23]</sup> The oxidation conditions in  $\text{CO}_2$  can be adjusted so that MXene is only partially converted to achieve ternary heterostructures such as  $\text{Nb}_2\text{C-C-Nb}_2\text{O}_5$ , resulting in significantly enhanced electrochemical<sup>[24]</sup> and photocatalytic<sup>[25]</sup> performances compared to the parent  $\text{Nb}_2\text{C}$ . These hierarchical heterostructures benefit from synergistic effects of a conductive

carbon/MXene network, a layered 2D MXene structure, and a transition metal oxide semiconductor, that is, making them electrochemically and/or catalytically active.

Recently, hybrids of MXene-transition metal sulfides have gained growing attention.<sup>[26]</sup> Examples include  $\text{Ti}_3\text{C}_2$ - $\text{MoS}_2$  hybrids fabricated either by chemical synthesis of  $\text{MoS}_2$  in the presence of  $\text{Ti}_3\text{C}_2$  MXene,<sup>[27, 28]</sup> or by physical admixing of the two.<sup>[29]</sup>  $\text{MoS}_2$  is part of the transition metal dichalcogenides (TMDs) class of 2D materials.<sup>[30]</sup> TMDs find extensive application in energy storage,<sup>[31]</sup> electrochemical desalination,<sup>[32]</sup> and electrocatalysis<sup>[33]</sup>. However, most TMDs suffer from low electrical conductivity and unfavorable strains during charge/discharge.<sup>[34]</sup> This translates to limited electron mobility to active sites and low stability upon cycling in electrocatalysis. Furthermore, a general problem of 2D structures is the reduced catalytic activity of the basal plane. Heterostructure engineering can significantly boost the catalytic properties of TMDs by improving conductivity, increasing edge terminations, activating the basal plane, or creating defects.<sup>[35]</sup> Therefore, heterostructures obtained by integrating TMDs and MXenes benefit from the latter's metallic conductivity, resulting in a more efficient charge transfer. This is shown by a six-fold enhancement of the hydrogen evolution reaction (HER) activity of  $\text{Ti}_3\text{C}_2$ - $\text{MoS}_2$  hybrid compared with sole  $\text{MoS}_2$  and a much larger enhancement than that of sole  $\text{Ti}_3\text{C}_2$ .<sup>[28]</sup> Nevertheless, the enhancement of the TMD-heterostructure properties is directly related to the interface quality of the heterojunction and minimization of Fermi level pinning.<sup>[26]</sup> A high hybridization degree can be achieved by converting or templating one of the heterostructure components into the other through atomic-scale transformation. MXene templating is still mostly limited to metal oxides.<sup>[36]</sup>

The direct conversion of MXene into TMD via in situ thermal sulfidation was so far explored to produce MXene-TMD heterostructures of  $\text{Mo}_2\text{TiC}_2$ - $\text{MoS}_2$ ,<sup>[37]</sup>  $\text{Mo}_2\text{C}$ - $\text{MoS}_2$ ,<sup>[38]</sup> and  $\text{Ti}_3\text{C}_2$ - $\text{TiS}_2$ ,<sup>[39]</sup> out of their parent delaminated MXenes. These MXene-derived TMDs are distributed in a unique sandwich-like fashion in the matrix of parent MXene. This morphology is accessible to electrolytes allowing for fast charge transfer. The intimate contact between the two phases provides strong adhesion and a nanohybrid interface<sup>[38]</sup> that is otherwise not achieved through TMD precursors' growth on MXene via other routes exemplified earlier. A variety of (mixed metal) MXenes remains unexplored as the precursor for TMD

fabrication. Furthermore, no study has been done comparing the effect of different MXene phases (e.g., with different  $n$ , such as comparing MXene with  $n=1$  to that of  $n=3$ ) on the resulting derivative of any kind.

The present study thus investigates the one-step thermal sulfidation technique for fabricating two niobium MXene-TMD heterostructures, namely  $\text{Nb}_2\text{C-NbS}_2$  and  $\text{Nb}_4\text{C}_3\text{-NbS}_2$ . Unlike other previous reports on MXene sulfidation, no delamination, pre-treatment with sulfur,<sup>[37, 38]</sup> or modification with carbon<sup>[39]</sup> were employed. The degree of the MXene-to-TMD conversion is shown to depend on the sulfidation temperature and duration, whereby hybrids of MXene- $\text{NbS}_2$  or only  $\text{NbS}_2$  structures could be conveniently obtained. The side-by-side comparison of structures derived from  $\text{Nb}_2\text{C}$  and  $\text{Nb}_4\text{C}_3$  MXenes reveals that each MXene undergoes unique conversion mechanisms, resulting in  $\text{NbS}_2$  with different nano-morphologies, such as pillars or mosaics. These heterostructures are further examined as electrocatalysts for HER.

## 2. Results and Discussion

The most common method of performing thermal sulfidation of different materials is by i) mixing the precursor with sulfur powder/sulfur salt,<sup>[40]</sup> which will likely react at higher temperatures or ii) placing sulfur powder upstream of the furnace, which in the form of vapor, upon heating, is carried to the main part of the furnace, where the precursor is located.  $\text{H}_2$  gas is often combined to form  $\text{H}_2\text{S}$  and facilitate the transfer.<sup>[41]</sup> These methods are limited by the amount of sulfur initially placed in the system and its evaporation rate. Above about 450 °C, sulfur quickly reacts with  $\text{H}_2$ , leading to a large amount of released  $\text{H}_2\text{S}$  in the first few minutes of the treatment, which quickly decreases due to sulfur depletion, leading to a heterogeneous feed rate of  $\text{H}_2\text{S}$  during treatment.<sup>[42]</sup> Direct use of  $\text{H}_2\text{S}$  gas, on the other hand, allows a constant flow and sulfur feed rate, providing more control over the sulfidation process, especially for longer treatment times (**Figure S1-S2**, Supporting Information).  $\text{Nb}_4\text{C}_3$  was treated by two different methods to verify this effect: directly using  $\text{H}_2\text{S}$  gas or reacting sulfur powder

with  $H_2$  upstream of the tube furnace. **Figure 1A** and **Figure S3, Supporting Information**, show the X-ray diffractograms of  $Nb_4C_3$  thermally treated with  $H_2S$  and  $H_2/S$  methods, respectively.

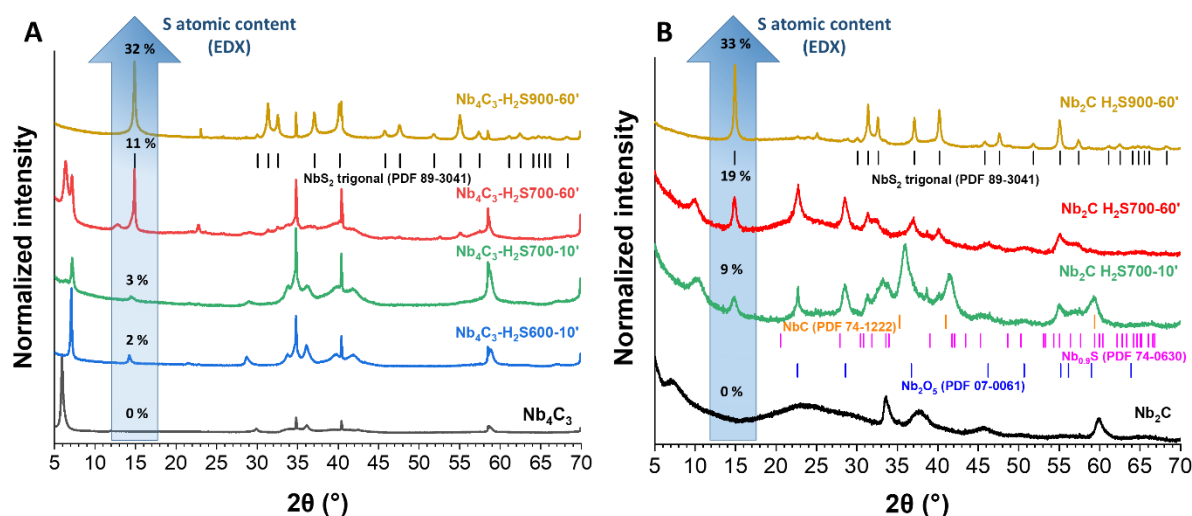


**Figure 1:** X-ray diffraction (XRD) patterns for the treatment in  $H_2S$  with (A)  $Nb_4C_3$  and (B)  $Nb_2C$ . The elemental values of sulfur were derived from energy-dispersive X-ray spectroscopy (EDX).

At 600 °C, no significant sulfidation is observed in either system, with only a broadening of MXene peaks. At 700 °C, a clear difference appears between the two methods. The sample treated with  $H_2S$  still shows the main features of MXene even at prolonged times ( $Nb_4C_3-H_2S700-60'$ ) with a pronounced broadening of the peaks. The (002) peak from MXene also shifts towards higher  $2\theta$  degree (**Table 1**), from  $5.93^\circ 2\theta$  ( $Nb_4C_3$ ) to  $7.10^\circ 2\theta$  ( $Nb_4C_3-H_2S600-10'$ ) and  $7.18^\circ 2\theta$  ( $Nb_4C_3-H_2S700-10'$ ), indicating a decrease in the interlayer spacing between the sheets. This change was already detected even when sulfidation did not occur (**Figure S3, Supporting Information**) at 500 °C and 600 °C, which can be explained by the removal of interlayer water and other etching products.<sup>[43]</sup> In the  $H_2/S$  setup, the sample clearly shows conversion to  $NbS_2$  matching the trigonal structure (PDF 89-3041), with no remaining peaks of the parent MXene when treated at 700 °C. The sharp differences between the two systems can be attributed to the amount of  $H_2S$  (and ultimately S) provided by each setup in the same time range (as qualitatively represented in **Figure S2B, Supporting Information**). This becomes obvious when the temperature increases to 900 °C, where the sample in  $H_2/S$  shows mainly  $NbS_2$  features within 10 min, while in  $H_2S$ , evidence of remaining  $Nb_4C_3$  is seen even after 60 min treatment.

The faster conversion rate in the H<sub>2</sub>/S system can also be verified by the sulfur content obtained by EDX analysis (**Table S1**, Supporting Information). The chemical composition obtained by EDX analysis corroborates the XRD data. The sulfur contents obtained by EDX analysis are cross-examined with CHNS elemental analysis, and the values are in close agreement with each other. No sulfur is detected below 600 °C while it reaches 31 at% when treated at 900 °C for 60 min. These changes are accompanied by decreased oxygen content and complete fluorine removal with increasing treatment temperature and time, confirming the (partial) removal of terminal functional groups from the MXene surface. The similar composition of Nb<sub>4</sub>C<sub>3</sub>-S900-10' and Nb<sub>4</sub>C<sub>3</sub>-S900-60' indicates that in this setup, complete conversion is already achieved in 10 min.

**Table 1:** MXene (002) peak position and ratio of (003)-NbS<sub>2</sub>/(002)-MXene peak area.

Sample	(002)-MXene (° 2 $\theta$ )	A <sub>sulfide</sub> /A <sub>MXene</sub>
Nb <sub>2</sub> C	7.27	0
Nb <sub>2</sub> C-H <sub>2</sub> S700-10'	10.47	0.49
Nb <sub>2</sub> C-H <sub>2</sub> S700-60'	10.02	1.18
Nb <sub>2</sub> C-H <sub>2</sub> S900-60'	-	-
Nb <sub>4</sub> C <sub>3</sub>	5.93	0
Nb <sub>4</sub> C <sub>3</sub> -H <sub>2</sub> S600-10'	7.10	0.16
Nb <sub>4</sub> C <sub>3</sub> -H <sub>2</sub> S700-10'	7.18	0.20
Nb <sub>4</sub> C <sub>3</sub> -H <sub>2</sub> S700-60'	6.39/7.16	0.62
Nb <sub>4</sub> C <sub>3</sub> -H <sub>2</sub> S900-60'	-	-
Nb <sub>4</sub> C <sub>3</sub> -S700-10'	-	-

The H<sub>2</sub>/S setup leads to faster conversion of the material. Hence, the partial conversion of the MXene becomes challenging. Partial conversion is highly desirable since a combination of the properties of the derived material and the parent MXene can be achieved, for example, the redox activity of metal oxides with the conductivity of MXene.<sup>[44]</sup> Besides, the fast conversion with H<sub>2</sub>/S method leads to heterogeneous reactions and the formation of coarsened particles spread within the original layered structure, as observed in scanning electron micrographs (**Figure S4**, Supporting Information). That considered, Nb<sub>2</sub>C phase was only treated with the H<sub>2</sub>S system.

For Nb<sub>2</sub>C, a similar change in composition occurs, ultimately leading to tetragonal NbS<sub>2</sub> at 900 °C in 60 min (**Figure 1B**). In this case, the transition seems to occur faster than in Nb<sub>4</sub>C<sub>3</sub>, as observed by comparing the percentage of sulfide incorporated (**Table S2**, Supporting Information) and the  $A_{\text{sulfide}}/A_{\text{MXene}}$  ratio (**Table 1**) in the different treatment conditions between the two MXene phases. This could be explained by the slightly larger surface area of the Nb<sub>2</sub>C-MXene than Nb<sub>4</sub>C<sub>3</sub>-MXene (**Figure S5**, Supporting Information), which enhances the exposure to the H<sub>2</sub>S, facilitating the conversion process. Similar to Nb<sub>4</sub>C<sub>3</sub>, Nb<sub>2</sub>C patterns also presented a shift of (002) peaks to higher angles after the heat treatments (**Table 1**).

Furthermore, the samples treated at 700 °C show reflections corresponding to Nb<sub>2</sub>O<sub>5</sub> in addition to Nb<sub>2</sub>C and NbS<sub>2</sub>. The Nb<sub>2</sub>O<sub>5</sub> formation in the case of Nb<sub>2</sub>C precursor can be explained by the higher atomic O/Nb ratio in Nb<sub>2</sub>C compared to Nb<sub>4</sub>C<sub>3</sub> (1.47 compared to 0.60, respectively; **Table S1-S2**, Supporting Information). During heat treatment, the large amount of oxygen promotes Nb oxidation in Nb<sub>2</sub>C, as not all functionalities are lost at 700 °C.<sup>[45]</sup>

The Nb<sub>2</sub>O<sub>5</sub> reflections remain even when the treatment is extended to 60 min at 700 °C (**Figure 1B**), indicating that the oxide neither decomposes nor is further converted during the treatment with H<sub>2</sub>S. Once Nb<sub>2</sub>O<sub>5</sub> is formed, its sulfidation is thermodynamically unfavored at 700 °C, requiring higher temperatures than Nb<sub>2</sub>C to form NbS<sub>2</sub>.<sup>[46]</sup> This can explain the absent Nb<sub>2</sub>O<sub>5</sub> signal in the Nb<sub>2</sub>C-H<sub>2</sub>S900-60' sample: the higher temperature efficiently removes surface functionalities. Besides, H<sub>2</sub>S decomposition is favored above 900 °C, leading to a more significant amount of H<sub>2</sub> that helps to reduce oxygenated groups.<sup>[42]</sup>



In case of the sample Nb<sub>2</sub>C-H<sub>2</sub>S700-10', in addition to the formation of NbS<sub>2</sub> and Nb<sub>2</sub>O<sub>5</sub>, a sharp reflection also appears at  $2\theta = 41.5^\circ$ . Although the latter reflection could not categorically be assigned to a certain phase, we speculate that it originates from cubic NbC and other niobium sulfide species such as Nb<sub>0.9</sub>S (**Figure 1B**). The rather short exposure time to H<sub>2</sub>S (10 min) can explain the formation of the latter sulfur-deficient niobium sulfide stoichiometry.

The scanning electron microscopy (SEM) images presented in **Figure 2** and **Figure S6**, Supporting Information, show the morphology of the materials before and after different sulfidation conditions. The original layered MXene structure is still observed for all samples, and the flake particles remain essentially of the same size. For treatments at 900 °C, such layers are mainly composed of hexagonal and trigonal nano-mosaics, characteristic of NbS<sub>2</sub> morphology. The gradual development of morphologies seen at 700 °C further leads to the morphologies seen at 900 °C (**Figure 2B-D**). At certain particles (**Figure 2B**), hexagons appear at the edge plane, with a higher surface and exposure to H<sub>2</sub>S gas. The same features are also seen at places where the layer-opening is more pronounced. Such morphologies are very different from the samples treated in H<sub>2</sub>/S setup (**Figure S4**, Supporting Information). Large rhombohedral particles appear on top and grow from the layers, resulting in a much more heterogeneous material.

A strikingly different feature occurs in the Nb<sub>2</sub>C treated at 700 °C (**Figure 2F** and **Figure S6D-F**, Supporting Information). Several pillars growing mainly from the basal plane are observed throughout the whole material. Such pillars occur between smaller layers and grow considerably at the external surface, up to 1 μm. When the reaction time is increased from 10 min (Nb<sub>2</sub>C-H<sub>2</sub>S700-10') to 60 min (Nb<sub>2</sub>C-H<sub>2</sub>S700-60'), the pillars seem to increase in quantity. At 900 °C (Nb<sub>2</sub>C-H<sub>2</sub>S900-60') however, there are no signs of such morphology, indicating that such structures are decomposed at higher temperatures.

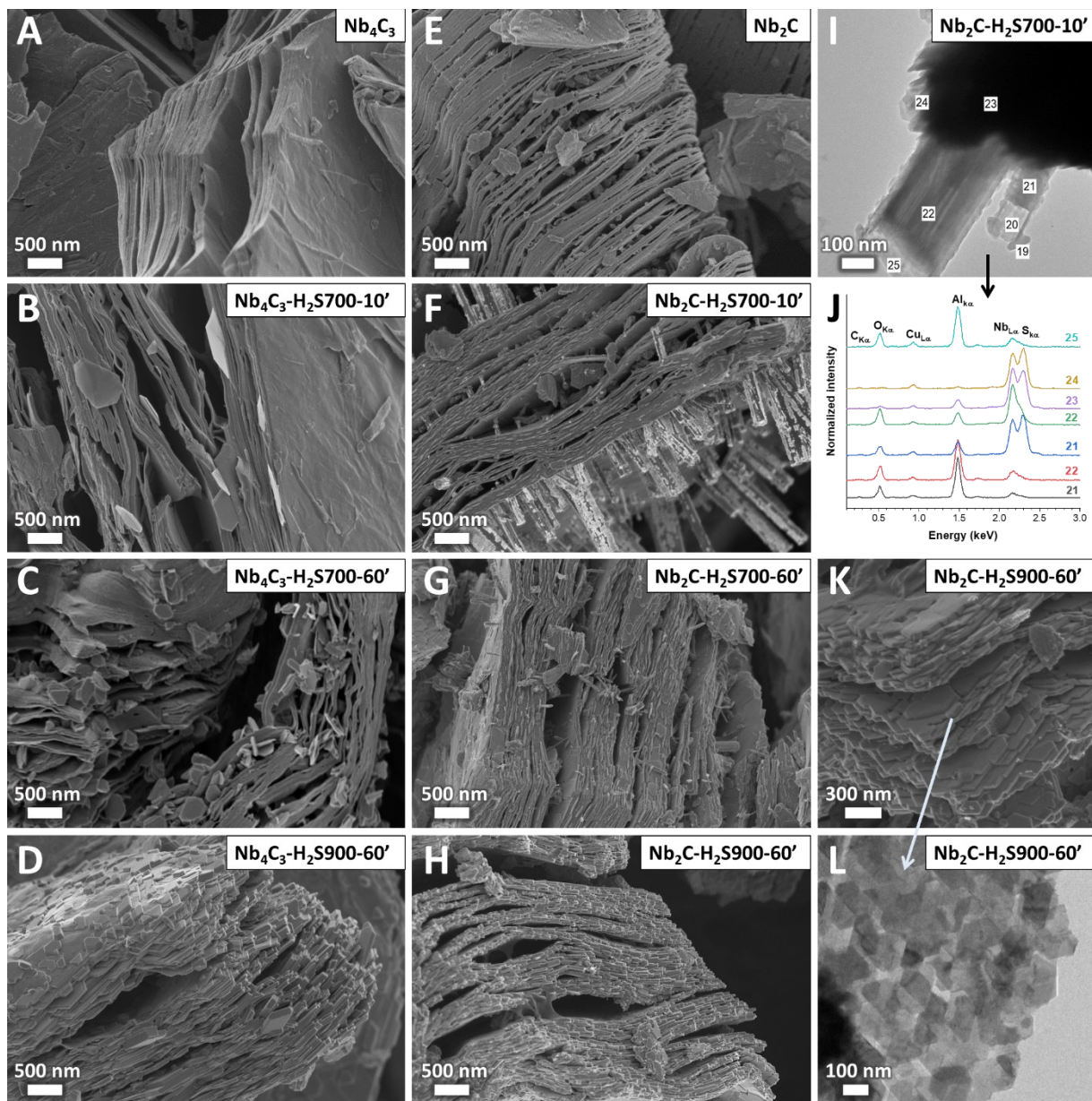


**Figure 2:** Scanning electron micrographs of (A)  $\text{Nb}_4\text{C}_3$ , (B)  $\text{Nb}_4\text{C}_3\text{-H}_2\text{S700-10'}$ , (C)  $\text{Nb}_4\text{C}_3\text{-H}_2\text{S700-60'}$ , (D)  $\text{Nb}_4\text{C}_3\text{-H}_2\text{S900-60'}$ , (E)  $\text{Nb}_2\text{C}$ , (F)  $\text{Nb}_2\text{C-H}_2\text{S700-10'}$ , (G)  $\text{Nb}_2\text{C-H}_2\text{S700-60'}$  and (H,K)  $\text{Nb}_2\text{C-H}_2\text{S900-60'}$ . Transmission electron micrographs of (I)  $\text{Nb}_2\text{C-H}_2\text{S700-10'}$  and (L)  $\text{Nb}_2\text{C-H}_2\text{S900-60'}$ . (J) Elemental composition via energy-dispersive X-ray spectroscopy of the assigned points in image (I).

To further investigate these morphologies, transmission electron microscopy (TEM) images were acquired (**Figure 2I, L; Figure S7**, Supporting Information). In the Nb<sub>2</sub>C-H<sub>2</sub>S900-60' the layers composed of prismatic NbS<sub>2</sub> nano-mosaics are nicely seen. The lattice spacing of 0.285 nm matches the (101) plane of NbS<sub>2</sub> also observed in XRD. The same structures occur for the Nb<sub>4</sub>C<sub>3</sub> sample treated under the same conditions. For Nb<sub>2</sub>C-H<sub>2</sub>S700-10' the pillars previously seen in SEM appear together with the layered material. The pillars seem to grow parallel to the basal plane in many regions, protruding from in-between the layers. The lattice spacing of the pillars is ca. 0.388 nm, 0.314 nm, and 0.250nm, which matches the (001), (100), and (101) reflections of Nb<sub>2</sub>O<sub>5</sub>, respectively. The base from where the pillars grow also shows organized spacing with ca. 0.62 nm and 0.285 nm matching the (003) and (101) reflections of NbS<sub>2</sub>, respectively. While other characterizations indicate the presence of residual MXene in this sample, it was not possible to identify characteristic spacings of Nb<sub>2</sub>C in this sample. Possibly the remaining MXene occurs at the inner layers of the material, which cannot be identified in TEM as only the edges and partially delaminated layers can be analyzed. Nevertheless, in Nb<sub>4</sub>C<sub>3</sub>-H<sub>2</sub>S700-10' sample, spacing corresponding to (002) plane of Nb<sub>4</sub>C<sub>3</sub> can be more easily found (**Figure S7A**, Supporting Information), confirming the partial conversion already observed in XRD.

EDX spectra also confirmed the composition (**Figure 2J**): while the layered particles are mainly composed of Nb and S, the pillars show the presence of Nb and O. Al appears at the far end/top of most of these structures, which could be part of the pillar growing mechanism acting as a catalyst. The evidence that the pillars observed in the Nb<sub>2</sub>C samples treated at 700 °C are composed of Nb<sub>2</sub>O<sub>5</sub> also aligns with XRD data (**Figure 1B**), since neither the pillars nor Nb<sub>2</sub>O<sub>5</sub> peaks are seen in Nb<sub>2</sub>C-H<sub>2</sub>S900-60'. To understand the decomposition mechanism of such pillars, Nb<sub>2</sub>C was heat-treated only in an inert atmosphere (Argon) up to 900 °C. In this condition, NbO<sub>2</sub> is observed (**Figure S8**, Supporting Information). This indicates that the oxide pillars were reduced upon temperature increase and only further reduced/converted during the sulfidation process with the introduction of H<sub>2</sub>S, leading to the absence of pillars or oxide in the Nb<sub>2</sub>C-H<sub>2</sub>S900-60' sample.

Raman spectra of Nb<sub>4</sub>C<sub>3</sub> and Nb<sub>2</sub>C treated with H<sub>2</sub>S are presented in **Figure S9** (Supporting Information). Before the treatment, Nb-C modes appear below 300 cm<sup>-1</sup>, corresponding to A<sub>1g</sub> out-of-plane vibration ( $\omega_4$ , ca. 260 cm<sup>-1</sup>) and E<sub>g</sub> in-plane oscillations ( $\omega_2$  ca. 180 cm<sup>-1</sup>)<sup>[47]</sup>. The functional terminations (Nb-F, Nb-O, Nb-OH) appear at 450-800 cm<sup>-1</sup>.<sup>[48]</sup> Compared to Nb<sub>4</sub>C<sub>3</sub>, Nb<sub>2</sub>C bands present a shift towards higher frequencies as M<sub>n+1</sub>X<sub>n</sub>-O tend to be stronger with the decrease of n. <sup>[49]</sup> The difference in the Nb-O bond strength could be one of the factors that lead to the growth of Nb<sub>2</sub>O<sub>5</sub> pillars in Nb<sub>2</sub>C and their absence in Nb<sub>4</sub>C<sub>3</sub>. These modes gradually disappear with increasing temperature and time as this bonding is broken to form NbS<sub>2</sub>. This transition is more abrupt in Nb<sub>2</sub>C as previously discussed that this phase has a faster conversion. With the treatment, typical modes of 2H-NbS<sub>2</sub> emerge at 386 cm<sup>-1</sup> (A<sub>1</sub>), 322 cm<sup>-1</sup> (E<sub>2</sub>), and 153 cm<sup>-1</sup> (defects).<sup>[50]</sup> Carbon modes are also present between 1200 cm<sup>-1</sup> and 1700 cm<sup>-1</sup>. The band at lower wavenumber (ca. 1350 cm<sup>-1</sup>) is defined as the D-band. It is associated with disordered amorphous sp<sup>3</sup> carbon, while the G-band at ca. 1600 cm<sup>-1</sup> is characteristic of graphitic sp<sup>2</sup> carbon mode.<sup>[51]</sup> For Nb<sub>4</sub>C<sub>3</sub>, C modes initially increase with treatment, as free C is formed while niobium is sulfidized.<sup>[52]</sup> The broadness of the D-band is further decreased when the temperature rises to 900° C, with a D-mode and G-mode typical of defective graphitic carbon formed at higher temperatures. Even at high temperatures, the presence of carbon modes suggests a hybrid structure between NbS<sub>2</sub>, carbon, and possibly residual MXene. Conversely, carbon modes are minimized and disappear upon treatment of Nb<sub>2</sub>C. The less shielding of niobium layers and the single carbon layer possessed by the 211 MAX-phase leads to less protection of the carbon atoms and further decomposition.

To understand the surface chemistry of Nb<sub>4</sub>C<sub>3</sub> before and after sulfidation and the nature of Nb at the surface, X-Ray photoelectron spectroscopy was studied for both Nb<sub>4</sub>C<sub>3</sub> (**Figure 3A, C, Figure S10A,C**, Supporting information) and Nb<sub>4</sub>C<sub>3</sub>-S900-60' (**Figure 3B,D, Figure S10B,D**, Supporting information). The data of both samples were calibrated using adventitious carbon (C-C/C-H at 284.8 eV). For Nb<sub>4</sub>C<sub>3</sub> sample, **Figure 3A** shows C 1s spectrum where the peak at 282.7 eV can be assigned to C-Nb in MXene.<sup>[53]</sup> **Figure 3C** shows the Nb 3d spectrum of Nb<sub>4</sub>C<sub>3</sub> where the doublet peaks at 203.8 eV and 206.6 eV are assigned to Nb-C in Nb<sub>4</sub>C<sub>3</sub> MXene. The doublets found at higher binding energies are

assigned to Nb-O of different oxidation states.<sup>[53]</sup> For Nb<sub>4</sub>C<sub>3</sub>-S900-60' sample, **Figure 3B**) shows C 1s spectrum where the C-Nb was not observed, which could be attributed to the NbS<sub>2</sub> nanomosaic layer formation upon sulfidation. For the Nb 3d spectrum of Nb<sub>4</sub>C<sub>3</sub>-S900-60' in **Figure 3D**, it is impossible to differentiate between Nb<sub>4</sub>C<sub>3</sub> and NbS<sub>2</sub> as the Nb-S, and Nb-C doublet peaks binding energies are too close to be distinguished from each other. Previous literature of Nb-S doublets were found at (203.4±0.2 eV and 206.1±0.2 eV) for 3R-NbS<sub>2</sub> and (204.0±0.2 eV and 206.7±0.2 eV) for 2H (or 1H) NbS<sub>2</sub>.<sup>[54]</sup> Since the C-Nb peak was not observed in the C 1s spectrum of Nb<sub>4</sub>C<sub>3</sub>-S900-60' surface, it is reasonable to assume that the Nb 3d spectrum does not include the Nb-C doublet. Therefore, we were able to assign (203.4 eV and 206.1 eV) to Nb<sup>+4</sup>-S in 3R-NbS<sub>2</sub> and (203.8 eV and 206.5 eV) to Nb<sup>+4</sup>-S in 2H-NbS<sub>2</sub>.<sup>[54]</sup>

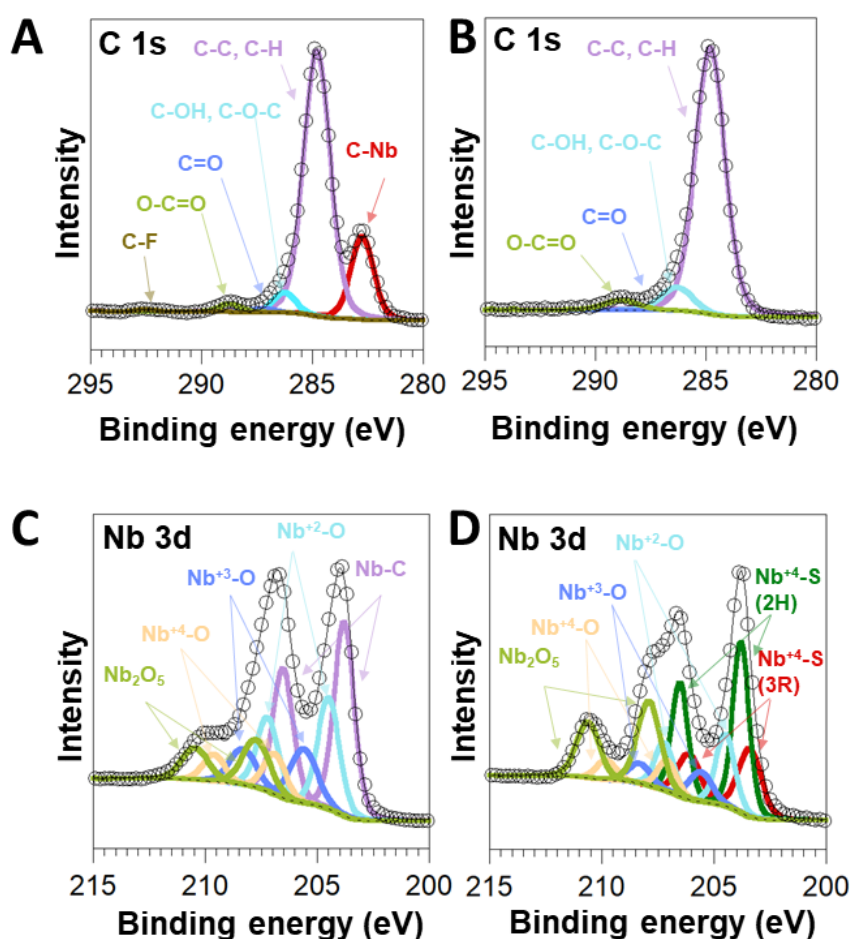


**Figure 3.** X-ray photoelectron spectra of C 1s of the pristine samples for (a) Nb<sub>4</sub>C<sub>3</sub>, and (b) Nb<sub>4</sub>C<sub>3</sub>-S900-60', and Nb 3d for (c) Nb<sub>4</sub>C<sub>3</sub>, and (d) Nb<sub>4</sub>C<sub>3</sub>-S900-60'.

We also studied the C 1s and Nb 3d spectra (**Figure S10A-B**, Supporting information) for both samples after sputtering to study the sub-surface chemistry. The C-Nb peak in C 1s spectrum relatively increased in Nb<sub>4</sub>C<sub>3</sub> (**Figure S10A**, Supporting information), but more importantly, it showed up in Nb<sub>4</sub>C<sub>3</sub>-S900-60' (**Figure S10B**, Supporting information). This reveals the existence of Nb<sub>4</sub>C<sub>3</sub> under the nanomosaic NbS<sub>2</sub> layer. The presence of Nb-C signal in Nb<sub>4</sub>C<sub>3</sub>-S900-60' sample after sputtering demonstrates that the conversion of the MXene into the sulfide take place from outer to inner layers. Furthermore, this indicates that the samples treated at milder conversion conditions (700 °C) are indeed partially converted and composed by MXene-NbS<sub>2</sub> hybrid. The Nb 3d spectra of both samples after sputtering (**Figure S10C-D**, Supporting information) reveal no Nb<sub>2</sub>O<sub>5</sub> peak at high binding energy. To investigate the electrocatalytic behaviors of the as-prepared samples, linear sweep voltammetry (LSV) was carried out in an H<sub>2</sub>-bubbled 0.5 M H<sub>2</sub>SO<sub>4</sub> aqueous electrolyte. As shown in **Figure 4A**, Nb<sub>4</sub>C<sub>3</sub> pristine, Nb<sub>4</sub>C<sub>3</sub>-H<sub>2</sub>S600-10', Nb<sub>4</sub>C<sub>3</sub>-H<sub>2</sub>S700-10', and Nb<sub>4</sub>C<sub>3</sub>-H<sub>2</sub>S900-60' exhibit similar electrocatalytic activities with almost the same onset-overpotentials. It can be seen that all samples show similar overpotentials of around 200 mV at 10 mA cm<sup>-2</sup>. A similar trend can be found for Nb<sub>2</sub>C-H<sub>2</sub>S700-10' and Nb<sub>2</sub>C-H<sub>2</sub>S900-60', in which the respective overpotentials of 250 mV and 252 mV are needed to deliver a current density of 10 mA cm<sup>-2</sup>. Given the lower overpotential for Nb<sub>4</sub>C<sub>3</sub> and Nb<sub>4</sub>C<sub>3</sub>-derived samples compared to Nb<sub>2</sub>C and its derived samples, we focus herein on the electrocatalytic behavior of the formers.

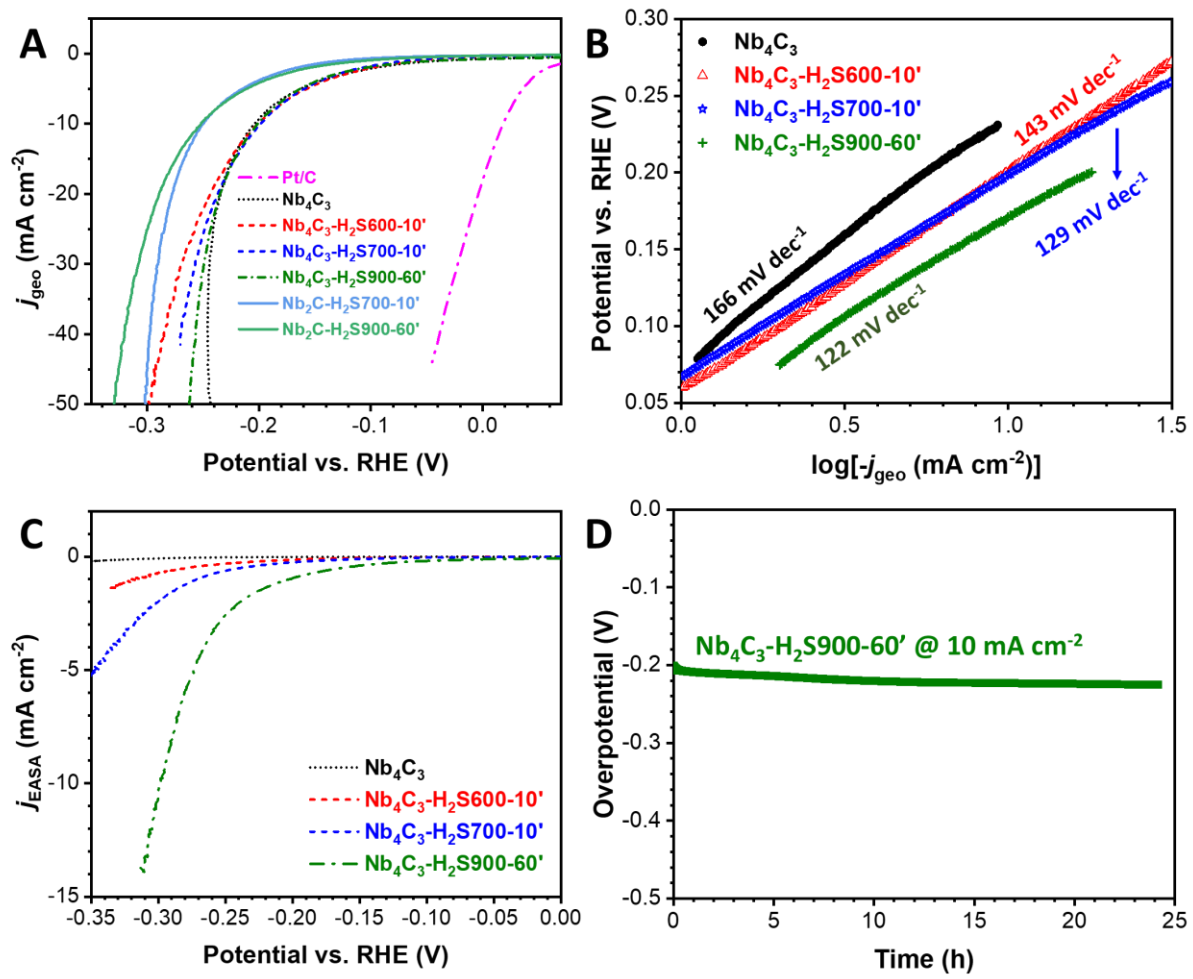


**Figure 4.** Electrocatalytic HER performance. A) iR-corrected LSV curves for HER measured at 5 mV s<sup>-1</sup> and (B) the corresponding Tafel slopes for Nb<sub>4</sub>C<sub>3</sub> pristine, Nb<sub>4</sub>C<sub>3</sub>-H<sub>2</sub>S600-10', Nb<sub>4</sub>C<sub>3</sub>-H<sub>2</sub>S700-10' and Nb<sub>4</sub>C<sub>3</sub>-H<sub>2</sub>S900-60', respectively. (C) iR-corrected LSV curves normalized to electrochemically active surface area (D) The long-term electrochemical stability of Nb<sub>4</sub>C<sub>3</sub>-H<sub>2</sub>S900-60' with a constant current density of 10 mA cm<sup>-2</sup>.

Generally, the following three possible pathways can be used to describe the HER mechanism in the acidic electrolyte (Eq. 2-3):<sup>[55]</sup>



where  $H_{ads}$  denotes the adsorption of H on the catalyst surface. Therefore, hydrogen can be generated by the Volmer-Heyrovsky step or the Volmer-Tafel step.

The Tafel slopes of Nb<sub>4</sub>C<sub>3</sub> pristine, Nb<sub>4</sub>C<sub>3</sub>-H<sub>2</sub>S600-10', Nb<sub>4</sub>C<sub>3</sub>-H<sub>2</sub>S700-10' and Nb<sub>4</sub>C<sub>3</sub>-H<sub>2</sub>S900-60' are calculated to be 166, 143, 129, and 122 mV dec<sup>-1</sup>, respectively (**Figure 4B**). The lower Tafel slope of Nb<sub>4</sub>C<sub>3</sub>-H<sub>2</sub>S900-60' indicates faster electron transfer than the others. The large Tafel slopes suggest that a Volmer-Heyrovsky step generated the hydrogen, and H (Volmer step) adsorption is the limiting step.<sup>[55]</sup>

To further study the HER activity, each sample's electrochemically active surface area (EASA) is calculated by performing cyclic voltammetry at different scan rates (**Figure S11**, Supporting Information). In this work, a non-Faradaic potential region with the center of open circuit potential is used. The open circuit potential varies from one sample to the other, so a different potential range is employed in this work to avoid any Faradic contribution from any of the samples for accurate estimation of the EASA. The EASA differs from BET specific surface area as the first determines the electrochemically available surface while the latter probes the area accessible for nitrogen physisorption.

The EASA values for Nb<sub>4</sub>C<sub>3</sub> pristine, Nb<sub>4</sub>C<sub>3</sub>-H<sub>2</sub>S600-10', Nb<sub>4</sub>C<sub>3</sub>-H<sub>2</sub>S700-10', and Nb<sub>4</sub>C<sub>3</sub>-H<sub>2</sub>S900-60' were obtained as 35.1 cm<sup>2</sup>, 5.1 cm<sup>2</sup>, 2.6 cm<sup>2</sup>, and 0.7 cm<sup>2</sup>, respectively. The EASA decreases significantly after treatments, and the higher temperatures result in smaller EASA values. The very high EASA of Nb<sub>4</sub>C<sub>3</sub> is attributed to the large *d*-spacing that renders the interlayer spacing accessible for ions and available for electrochemical processes. The reduction in EASA upon treatment can be explained by collapsing MXene's interlayer spacing during the heating cycle. Unlike normalizing the current by geometric area of the electrode, normalizing by the specific surface area or EASA reflects the intrinsic catalytic activity of the material rather than size dependence.<sup>[56]</sup> When LSV curves are normalized to EASA (**Figure 4C**), the Nb<sub>4</sub>C<sub>3</sub>-H<sub>2</sub>S900-60' sample shows the highest HER activity. This suggests that even though this sample has lower EASA, it is intrinsically much more catalytically active than untreated MXene. Therefore, further enhancement in the kinetics of the HER is expected for Nb<sub>4</sub>C<sub>3</sub>-H<sub>2</sub>S900-60' in the future by approaches to increase its EASA, such as milling.



**Table S3** (Supporting Information) lists the electrocatalytic performance of various NbS<sub>2</sub> morphologies employed as HER catalysts in recent literature. The Nb<sub>4</sub>C<sub>3</sub>-H<sub>2</sub>S900-60' in the present work shows a relatively low overpotential (198 mV at 10 mA cm<sup>-2</sup>) and Tafel slope (122 mV dec<sup>-1</sup>), revealing higher electrocatalytic activity than most of the reported NbS<sub>2</sub> and MXenes as HER catalysts. The improved performance of the latter sample can be attributed to the nanoscale mosaic morphology achieved where more edges are exposed. The long-term electrocatalytic stability was conducted in a 0.5 M H<sub>2</sub>SO<sub>4</sub> electrolyte with a current density of 10 mA cm<sup>-2</sup> for 24 h. As shown in **Figure 4D**, Nb<sub>4</sub>C<sub>3</sub>-H<sub>2</sub>S900-60' exhibits promising electrochemical stability.

### 3. Conclusions

In summary, heterostructures of MXene-TMD were obtained by a one-step thermal sulfidation of niobium MXenes. Our work for the first time demonstrated that by a facile manipulation of the treatment temperature and duration, different degrees of MXene-to-TMD conversion is obtained. It has been shown that the parent MXene slab thickness plays a crucial role in the derived TMD nanostructure. Nb<sub>2</sub>C MXene is more susceptible to conversion into NbS<sub>2</sub> than Nb<sub>4</sub>C<sub>3</sub> MXene when treated at 700 °C for 10 min due to higher H<sub>2</sub>S exposure of Nb-C-Nb layers in Nb<sub>2</sub>C rather than Nb-C-Nb-C-Nb-C-Nb layers in Nb<sub>4</sub>C<sub>3</sub>. Tuning treatment conditions yielded various nanostructures depending on the MXene type, such as pillars in Nb<sub>2</sub>C and mosaics in the case of Nb<sub>4</sub>C<sub>3</sub> MXene. The treatment at 700 °C resulted in MXene-NbS<sub>2</sub> hybrids, whereas treatment at 900 °C for 60 min resulted in the complete conversion of MXene into NbS<sub>2</sub> nano-mosaics. Overall, the H<sub>2</sub>S gas method has better control over the conversion degree than the H<sub>2</sub> gas + S powder method.

When used as electrodes for HER, the Nb<sub>4</sub>C<sub>3</sub> MXene treated in H<sub>2</sub>S gas at 900 °C for 60 min exhibited the highest HER activity among all samples tested and promising cycling stability. Our study encourages the possibility of constructing a plethora of MXene-based TMD heterostructures for use as electrode materials for energy storage and conversion, among other applications. Further fine-tuning the derivatization parameters to optimize the electrochemical performance of the produced

heterostructures in future work may provide the path towards applications in more complex electrocatalytic applications and improved performances.

#### 4. Experimental Section

*Synthesis of Nb<sub>2</sub>AlC and Nb<sub>4</sub>AlC<sub>3</sub> MAX phases:* Nb<sub>2</sub>C and Nb<sub>4</sub>C<sub>3</sub> were synthesized by selective etching of the Al from their parent MAX phases, Nb<sub>2</sub>AlC and Nb<sub>4</sub>AlC<sub>3</sub>, respectively. Nb<sub>2</sub>AlC and Nb<sub>4</sub>AlC<sub>3</sub> were prepared via solid-state synthesis processes by mixing niobium (Nb, Alfa Aesar, <45 μm, 99.8 %), aluminum (Al, Alfa Aesar, 7-15 μm, 99.5 %), and carbon (C, Alfa Aesar, 7-11 μm, 99 %) with atomic ratios of 2:1.3:0.95 and 4:1.5:2.7, respectively. Each mixture was added to yttria-stabilized zirconia balls in a high-density polyethylene jar and was mixed using a Turbula mixer for 3 h at 56 rpm. The samples were then pressed at room temperature into pellets. Nb<sub>2</sub>AlC pellets were heated from room temperature to 1600 °C. The samples were held at the peak temperature for 4 h, then left to cool naturally to room temperature. Nb<sub>4</sub>AlC<sub>3</sub> pellets were heated through a three-temperature-step program: first at 750 °C for 30 min, second at 1450 °C for 30 min, and third at 1700 °C for 1 h. The heating rate used for both samples was 300 °C/h. All the heating and cooling steps were in an alumina tube furnace under a continuous flow of argon (Ar) with a flow rate of 100 sccm.

*Synthesis of Nb<sub>2</sub>C and Nb<sub>4</sub>C<sub>3</sub> MXenes:* Both Nb<sub>2</sub>AlC and Nb<sub>4</sub>AlC<sub>3</sub> were etched using hydrofluoric acid (48-51 % by mass HF, Acros Organics, 10 mL for each 1 g of MAX powder). The mixtures were heated to 40 °C in an oil bath, mechanically agitated using Teflon coated magnetic stirrer, and held for 90 h. Afterward, the products were washed with de-ionized (DI) water to remove the acid and etching side-products. The washing procedure starts with dividing the mixture into several centrifuging tubes (one tube for each 0.5 g of starting MAX phase), centrifuging at 3500 rpm for 5 min, discarding the supernatant, refilling the tube with DI water, and finally redispersing the sediment using vortex machine. This washing step was repeated several times until the pH level exceeded a value of 6. Finally, the as-prepared product was dried using vacuum-assisted filtration overnight.

*MXene sulfidation:* Nb<sub>4</sub>C<sub>3</sub> was placed in a quartz crucible inside a quartz tube positioned in a one-zone furnace. Two different methods were used to perform the sulfidation, named H<sub>2</sub>/S and H<sub>2</sub>S (**Figure S1**, Supporting Information).

Method H<sub>2</sub>/S: To produce H<sub>2</sub>S gas, a second crucible containing sulfur (S) powder was placed upstream in the tube outside the furnace, with a heating jacket fixed around it. The system was purged with Ar at 100 sccm for 2 h, heated at a rate of 300 °C/h to the target temperature (700 °C or 900 °C) with holding times of 10 min or 60 min. The Ar flow was kept at 50 sccm during heating, holding, and cooling steps. 20 min before reaching the holding temperature, H<sub>2</sub> gas flow was started at 10 sccm and turned off after holding time. Throughout the H<sub>2</sub> flow period, the heating jacket was kept at 550 °C (**Figure S2A**, Supporting Information).

Method H<sub>2</sub>S: Like method H<sub>2</sub>/S, initial purging, Ar flow, heating rates, and temperatures were kept the same. H<sub>2</sub>S gas was directly used instead of the combination of H<sub>2</sub> + S powder. H<sub>2</sub>S gas was initiated when the target temperature was reached and kept flowing during holding time at 50 sccm. The samples were named according to the target temperature and holding time, “S” for method H<sub>2</sub>/S, and “H<sub>2</sub>S” for method H<sub>2</sub>S. For example, Nb<sub>4</sub>C<sub>3</sub>-S700-10’ stands for Nb<sub>4</sub>C<sub>3</sub> sulfidized at 700 °C for 10 min in H<sub>2</sub>/S system. Nb<sub>4</sub>C<sub>3</sub>-H<sub>2</sub>S900-60’ stands for Nb<sub>4</sub>C<sub>3</sub> sulfidized at 900 °C for 60 min with H<sub>2</sub>S gas. For the sulfidation of Nb<sub>2</sub>C, only method H<sub>2</sub>S was applied, and the nomenclature follows the same pattern.

*Material characterization:* Scanning electron microscopy (SEM) was carried out using a ZEISS-Gemini SEM500 system coupled to an energy-dispersive X-ray (EDX) detector (Oxford Instruments for EDX analysis). Acceleration voltages of 1-3 kV were used for imaging and 15 kV for spectroscopy. The samples were analyzed without any conductive sputtering.

Transmission electron microscopy (TEM, JEOL 2100F) was performed at an acceleration voltage of 200 kV. The samples were dispersed in ethanol by tip sonication for 30 s, drop-cast onto a copper grid coated with a lacey carbon film, and dried at room temperature overnight.

X-ray diffraction (XRD) was conducted with a D8 Advance diffractometer (Bruker AXS) with a copper source (Cu-Kα, 40 kV, 40 mA). Signal was collected using a 1D Lynxeye detector at 0.02 2θ step with a rate of 1 s/step.

X-ray photoelectron spectroscopy (XPS) measurements were performed using the Thermo-Fisher K-Alpha Plus XPS. An air-free holder is used during the whole process to protect the samples from oxidation. The photon source was a monochromatized Al K  $\alpha$  line ( $h\nu = 1486.6$  eV). The spectra were acquired using a spot size of 400  $\mu\text{m}$ . A flood gun with combined electrons and low energy Ar ions was used during the measurements. A dual monoatomic and gas cluster Argon ion source was used for depth profiling and sample cleaning.

Raman spectra (Renishaw inVia Raman microscope) were acquired with an Nd-YAG laser (532 nm) at 0.5 mW power with 10 s acquisition time for 10 accumulations using an objective lens with a numeric aperture of 0.75. At least 12 points were collected for each sample. The data show a representative spectrum of each sample.

Nitrogen gas sorption measurements were performed with an Autosorb iQ system (Quantachrome, Anton Paar) at  $-196$  °C. The  $\text{Nb}_2\text{C}$  and  $\text{Nb}_4\text{C}_3$  samples were first degassed at  $200$  °C at  $10^2$  Pa for one day. The specific surface areas were calculated by applying the Brunauer-Emmett-Teller (BET) model<sup>[57]</sup> within the linear pressure range (up to 0.3 relative pressure)<sup>[58]</sup>.

Elemental analysis (CHNS) was performed with Vario Micro Cube System using sulfanilamide for calibration and a reduction temperature of  $850$  °C. An OXY cube oxygen analyzer at  $1450$  °C was employed for the quantitative analysis of elemental oxygen.

*Electrochemical measurements:* The electrochemical performance was conducted by a Bio-Logic SP200 portable electrochemical workstation with an RRDE-3A rotating ring disk electrode system. A standard SVC-2 three-electrode system with a working electrode of as-prepared samples, a  $\text{Hg}/\text{Hg}_2\text{SO}_4$  electrode with saturated KCl supporting solution as a reference electrode, and a graphite rod as a counter electrode were used to investigate the hydrogen evolution activity in  $0.5$  M  $\text{H}_2\text{SO}_4$  aqueous electrolyte. The working electrode was prepared by dispersing the as-prepared materials (10 mg) in a mixture of 750  $\mu\text{L}$  water, 250  $\mu\text{L}$  ethanol, and 10  $\mu\text{L}$  Nafion 117 solution ( $\sim 5$  % in a mixture of lower aliphatic alcohols and water, Sigma Aldrich), followed by 1 h sonication. After that, 7  $\mu\text{L}$  dispersion was drop-cast on the glassy carbon electrode and dried at room temperature. The mass loading of active materials was  $\sim 1$  mg  $\text{cm}^{-2}$ . Linear sweep voltammetry (LSV) was measured at  $5$  mV  $\text{s}^{-1}$  by rotating the

working electrode at 1600 rpm with flowing H<sub>2</sub> in the electrolyte. All LSV curves were *iR*-corrected, and the potentials were converted in reference to a reversible hydrogen electrode (RHE).

The CV polarization curves are used to calculate the electrochemically active surface area (EASA). EASA values were obtained from the hydrogen adsorption/desorption region, so only the double-layer charging current is used. In this work, a non-Faradaic potential region with the center of open circuit potential is used. EASA was estimated from the electrical double-layer capacitance (*C<sub>dl</sub>*) of the as-prepared materials. The *C<sub>dl</sub>* was analyzed via cyclic voltammetry with scan rates of 20-100 mV s<sup>-1</sup>.

The EASA was calculated using **Eq. (1)**:<sup>[59]</sup>

$$\text{EASA} = (C_{\text{dl}} \cdot A) / C_s \quad (1)$$

where *A* is the geometric area of the electrode, and *C<sub>s</sub>* is the capacitance from a smooth planar surface per unit area. An average value of *C<sub>s</sub>* = 40 μF cm<sup>-2</sup> is used in this work.<sup>[59]</sup>

## Supporting Information

Supporting Information is available from the Wiley Online Library or from the author.

## Acknowledgments

We acknowledge funding by the German Research Foundation (DFG, Deutsche Forschungsgemeinschaft) of the electroMOXene project (PR-1173/9) and the MXene-CDI project (PR-1173/11). The INM authors thank Eduard Arzt (INM) for his continuing support. Research at TU was supported by the National Science Foundation under Grant No. DMR-2048164.

## Conflict of Interest

The authors declare no conflict of interest.

## Data Availability Statement

Research data are not shared.

## References

- [1] M. W. Barsoum, *MAX phases: Properties of machinable ternary carbides and nitrides*, Wiley, 2013.
- [2] M. Naguib, M. Kurtoglu, V. Presser, J. Lu, J. Niu, M. Heon, L. Hultman, Y. Gogotsi, M. W. Barsoum, *Adv. Mater.* 2011, 23, 4248.
- [3] M. Naguib, O. Mashtalir, J. Carle, V. Presser, J. Lu, L. Hultman, Y. Gogotsi, M. W. Barsoum, *ACS Nano* 2012, 6, 1322.
- [4] M. Naguib, V. N. Mochalin, M. W. Barsoum, Y. Gogotsi, *Adv. Mater.* 2014, 26, 992.
- [5] M. Naguib, J. Halim, J. Lu, K. M. Cook, L. Hultman, Y. Gogotsi, M. W. Barsoum, *J. Am. Chem. Soc.* 2013, 135, 15966; M. R. Lukatskaya, O. Mashtalir, C. E. Ren, Y. Dall'Agnese, P. Rozier, P. L. Taberna, M. Naguib, P. Simon, M. W. Barsoum, Y. Gogotsi, *Science* 2013, 341, 1502; M. Naguib, J. Come, B. Dyatkin, V. Presser, P. L. Taberna, P. Simon, M. W. Barsoum, Y. Gogotsi, *Electrochem. Commun.* 2012, 16, 61.
- [6] A. D. Handoko, K. D. Fredrickson, B. Anasori, K. W. Convey, L. R. Johnson, Y. Gogotsi, A. Vojvodic, Z. W. Seh, *ACS Appl. Energy Mater.* 2017, 1, 173.
- [7] Z. W. Seh, K. D. Fredrickson, B. Anasori, J. Kibsgaard, A. L. Strickler, M. R. Lukatskaya, Y. Gogotsi, T. F. Jaramillo, A. Vojvodic, *ACS Energy Lett.* 2016, 1, 589.
- [8] E. Muckley, M. Naguib, I. N. Ivanov, *Nanoscale* 2018, 10, 21689; P. A. Rasheed, R. P. Pandey, T. Gomez, M. Naguib, K. A. Mahmoud, *RSC Adv.* 2020, 10, 24697; X. Zhu, B. Liu, H. Hou, Z. Huang, K. M. Zeinu, L. Huang, X. Yuan, D. Guo, J. Hu, J. Yang, *Electrochim. Acta* 2017, 248, 46.
- [9] K. Rasool, R. P. Pandey, P. A. Rasheed, S. Buczek, Y. Gogotsi, K. A. Mahmoud, *Mater. Today* 2019, 30, 80; M. Torkamanzadeh, L. Wang, Y. Zhang, O. z. Budak, P. Srimuk, V. Presser, *ACS Appl. Mater. Interfaces* 2020, 12, 26013.
- [10] O. Mashtalir, M. Naguib, V. N. Mochalin, Y. Dall'Agnese, M. Heon, M. W. Barsoum, Y. Gogotsi, *Nat. Commun.* 2013, 4, 1716.
- [11] A. Shayesteh Zeraati, S. A. Mirkhani, P. Sun, M. Naguib, P. V. Braun, U. Sundararaj, *Nanoscale* 2021, 13, 3572.
- [12] H. Wang, J.-M. Lee, *J. Mater. Chem. A* 2020, 8, 10604.
- [13] S. Husmann, O. Budak, H. Shim, K. Liang, M. Aslan, A. Kruth, A. Quade, M. Naguib, V. Presser, *Chem. Commun.* 2020, 56, 11082; V. Natsu, R. Pai, M. Sokol, M. Carey, V. Kalra, M. W. Barsoum, *Chem* 2020, 6, 616; A. Jawaid, A. Hassan, G. Neher, D. Nepal, R. Pachter, W. J. Kennedy, S. Ramakrishnan, R. A. Vaia, *ACS Nano* 2021, 15, 2771; W. Sun, S. Shah, Y. Chen, Z. Tan, H. Gao, T. Habib, M. Radovic, M. Green, *J. Mater. Chem. A* 2017, 5, 21663; M. Ghidui, M. R. Lukatskaya, M. Q. Zhao, Y. Gogotsi, M. W. Barsoum, *Nature* 2014, 516, 78; Y. Li, H. Shao, Z. Lin, J. Lu, L. Liu, B. Duployer, P. O. Å. Persson, P. Eklund, L. Hultman, M. Li, K. Chen, X.-H. Zha, S. Du, P. Rozier, Z. Chai, E. Raymundo-Piñero, P.-L. Taberna, P. Simon, Q. Huang, *Nat. Mater.* 2020, 19, 894.
- [14] M. A. Hope, A. C. Forse, K. J. Griffith, M. R. Lukatskaya, M. Ghidui, Y. Gogotsi, C. P. Grey, *Phys. Chem. Chem. Phys.* 2016, 18, 5099.
- [15] A. Feng, Y. Yu, F. Jiang, Y. Wang, L. Mi, Y. Yu, L. Song, *Ceram. Int.* 2017, 43, 6322.
- [16] M. Li, J. Lu, K. Luo, Y. Li, K. Chang, K. Chen, J. Zhou, J. Rosen, L. Hultman, P. Eklund, P. O. Å. Persson, S. Du, Z. Chai, Z. Huang, Q. Huang, *J. Am. Chem. Soc.* 2019, 141, 4730.
- [17] T. Li, L. Yao, Q. Liu, J. Gu, R. Luo, J. Li, X. Yan, W. Wang, P. Liu, B. Chen, W. Zhang, W. Abbas, R. Naz, D. Zhang, *Angew. Chem., Int. Ed.* 2018, 57, 6115.
- [18] L. Verger, V. Natsu, M. Ghidui, M. W. Barsoum, *J. Phys. Chem. C* 2019, 123, 20044.
- [19] A. Al-Temimy, K. Prenger, R. Golnak, M. Lounasvuori, M. Naguib, T. Petit, *ACS Appl. Mater. Interfaces* 2020, 12, 15087.
- [20] J. Luo, W. Zhang, H. Yuan, C. Jin, L. Zhang, H. Huang, C. Liang, Y. Xia, J. Zhang, Y. Gan, X. Tao, *ACS Nano* 2017, 11, 2459.
- [21] W. Tian, A. VahidMohammadi, Z. Wang, L. Ouyang, M. Beidaghi, M. M. Hamedi, *Nat. Commun.* 2019, 10, 2558.

- [22] P. A. Maughan, V. R. Seymour, R. Bernardo-Gavito, D. J. Kelly, S. Shao, S. Tantisriyanurak, R. Dawson, S. J. Haigh, R. J. Young, N. Tapia-Ruiz, N. Bimbo, *Langmuir* 2020, 36, 4370; K. Liang, R. A. Matsumoto, W. Zhao, N. C. Osti, I. Popov, B. P. Thapaliya, S. Fleischmann, S. Misra, K. Prenger, M. Tyagi, E. Mamontov, V. Augustyn, R. R. Unocic, A. P. Sokolov, S. Dai, P. T. Cummings, M. Naguib, *Adv. Funct. Mater.* 2021, 31, 2104007.
- [23] M. Naguib, O. Mashtalir, M. R. Lukatskaya, B. Dyatkin, C. Zhang, V. Presser, Y. Gogotsi, M. W. Barsoum, *Chem. Commun.* 2014, 50, 7420.
- [24] C. F. Zhang, M. Beidaghi, M. Naguib, M. R. Lukatskaya, M. Q. Zhao, B. Dyatkin, K. M. Cook, S. J. Kim, B. Eng, X. Xiao, D. H. Long, W. M. Qiao, B. Dunn, Y. Gogotsi, *Chem. Mater.* 2016, 28, 3937.
- [25] T. Su, R. Peng, Z. D. Hood, M. Naguib, I. N. Ivanov, J. K. Keum, Z. Qin, Z. Guo, Z. Wu, *ChemSusChem* 2018, 11, 688.
- [26] N. R. Hemanth, T. Kim, B. Kim, A. H. Jadhav, K. Lee, N. K. Chaudhari, *Mater. Chem. Front.* 2021, 5, 3298.
- [27] M. Xu, N. Bai, H.-X. Li, C. Hu, J. Qi, X.-B. Yan, *Chin. Chem. Lett.* 2018, 29, 1313; X. Wu, Z. Wang, M. Yu, L. Xiu, J. Qiu, *Adv. Mater.* 2017, 29, 1607017.
- [28] L. Huang, L. Ai, M. Wang, J. Jiang, S. Wang, *Int. J. Hydrogen Energy* 2019, 44, 965.
- [29] C. Wang, X.-D. Zhu, K.-X. Wang, L.-L. Gu, S.-Y. Qiu, X.-T. Gao, P.-J. Zuo, N.-Q. Zhang, *Sustainable Energy Fuels* 2019, 3, 2577; Y. Wu, P. Nie, L. Wu, H. Dou, X. Zhang, *Chem. Eng. J.* 2018, 334, 932.
- [30] H. Wang, X. Xiao, S. Liu, C.-L. Chiang, X. Kuai, C.-K. Peng, Y.-C. Lin, X. Meng, J. Zhao, J. Choi, Y.-G. Lin, J.-M. Lee, L. Gao, *J. Am. Chem. Soc.* 2019, 141, 18578.
- [31] L. Lin, S. Zhang, D. A. Allwood, in *Two Dimensional Transition Metal Dichalcogenides: Synthesis, Properties, and Applications*, (Eds: N. S. Arul, V. D. Nithya), Springer Singapore, Singapore 2019, 173.
- [32] P. Srimuk, J. Lee, S. Fleischmann, S. Choudhury, N. Jäckel, M. Zeiger, C. Kim, M. Aslan, V. Presser, *J. Mater. Chem. A* 2017, 5, 15640.
- [33] Q. Fu, J. Han, X. Wang, P. Xu, T. Yao, J. Zhong, W. Zhong, S. Liu, T. Gao, Z. Zhang, L. Xu, B. Song, *Adv. Mater.* 2021, 33, 1907818.
- [34] C. Zhu, X. Mu, P. A. van Aken, Y. Yu, J. Maier, *Angew. Chem., Int. Ed.* 2014, 126, 2184.
- [35] P. Prabhu, V. Jose, J.-M. Lee, *Matter* 2020, 2, 526; Q. Yu, Y. Luo, A. Mahmood, B. Liu, H.-M. Cheng, *Electrochemical Energy Reviews* 2019, 2, 373.
- [36] L. Yu, B. Liu, Y. Wang, F. Yu, J. Ma, *J. Power Sources* 2021, 490, 229250.
- [37] C. Chen, X. Xie, B. Anasori, A. Sarycheva, T. Makaryan, M. Zhao, P. Urbankowski, L. Miao, J. Jiang, Y. Gogotsi, *Angew. Chem., Int. Ed.* 2018, 57, 1846.
- [38] K. R. G. Lim, A. D. Handoko, L. R. Johnson, X. Meng, M. Lin, G. S. Subramanian, B. Anasori, Y. Gogotsi, A. Vojvodic, Z. W. Seh, *ACS Nano* 2020, 14, 16140.
- [39] X. Huang, J. Tang, B. Luo, R. Knibbe, T. Lin, H. Hu, M. Rana, Y. Hu, X. Zhu, Q. Gu, D. Wang, L. Wang, *Adv. Energy Mater.* 2019, 9, 1901872; J. Tang, X. Huang, T. Lin, T. Qiu, H. Huang, X. Zhu, Q. Gu, B. Luo, L. Wang, *Energy Storage Mater.* 2020, 26, 550.
- [40] R. Tan, J. Yang, J. Hu, K. Wang, Y. Zhao, F. Pan, *Chem. Commun.* 2016, 52, 986; L. Fei, Y. Jiang, Y. Xu, G. Chen, Y. Li, X. Xu, S. Deng, H. Luo, *J. Power Sources* 2014, 265, 1; X. Yang, F. Xiao, S. Wang, J. Liu, M. K. H. Leung, D. Y. W. Yu, A. L. Rogach, *J. Mater. Chem. A* 2019, 7, 11877.
- [41] C.-F. Du, Q. Liang, Y. Zheng, Y. Luo, H. Mao, Q. Yan, *ACS Appl. Mater. Interfaces* 2018, 10, 33779; A. Frank, T. Gänsler, S. Hieke, S. Fleischmann, S. Husmann, V. Presser, C. Scheu, *Nanoscale Adv.* 2021, 3, 1067; S. Husmann, Ö. Budak, A. Quade, A. Frank, A. Kruth, C. Scheu, A. Tolosa, V. Presser, *J. Power Sources* 2020, 450, 227674; S. Fleischmann, T. S. Dörr, A. Frank, S. W. Hieke, D. Doblas-Jimenez, C. Scheu, P. W. de Oliveira, T. Kraus, V. Presser, *Batteries Supercaps* 2019, 2, 668; S. Choudhury, M. Zeiger, P. Massuti-Ballester, S. Fleischmann, P. Formanek, L. Borchardt, V. Presser, *Sustainable Energy Fuels* 2017, 1, 84.
- [42] N. I. Dowling, P. D. Clark, *Ind. Eng. Chem. Res.* 1999, 38, 1369.
- [43] J. L. Hart, K. Hantanasirisakul, A. C. Lang, B. Anasori, D. Pinto, Y. Pivak, J. T. van Omme, S. J. May, Y. Gogotsi, M. L. Taheri, *Nat. Commun.* 2019, 10, 522; I. Persson, L.-Å. Näslund, J. Halim, M. W. Barsoum, V. Darakchieva, J. Palisaitis, J. Rosen, P. O. Å. Persson, *2D Mater.* 2017, 5, 015002.

- [44] C. Zhang, S. J. Kim, M. Ghidui, M.-Q. Zhao, M. W. Barsoum, V. Nicolosi, Y. Gogotsi, *Adv. Funct. Mater.* 2016, 26, 4143; M. Zhang, X. Chen, J. Sui, B. S. Abraha, Y. Li, W. Peng, G. Zhang, F. Zhang, X. Fan, *Inorg. Chem. Front.* 2020, 7, 1205.
- [45] M. Seredych, C. E. Shuck, D. Pinto, M. Alhabeib, E. Precetti, G. Deysher, B. Anasori, N. Kurra, Y. Gogotsi, *Chem. Mater.* 2019, 31, 3324.
- [46] A. Mansouri, N. Semagina, *ACS Catal.* 2018, 8, 7621.
- [47] H. Lin, S. Gao, C. Dai, Y. Chen, J. Shi, *J. Am. Chem. Soc.* 2017, 139, 16235; N. J. Lane, M. Naguib, V. Presser, G. Hug, L. Hultman, M. W. Barsoum, *J. Raman Spectrosc.* 2012, 43, 954.
- [48] E. Capelli, R. Konings, *J. Fluorine Chem.* 2018, 208, 55; T. Hu, J. Wang, H. Zhang, Z. Li, M. Hu, X. Wang, *Phys. Chem. Chem. Phys.* 2015, 17, 9997.
- [49] M. Magnuson, J. Halim, L.-Å. Näslund, *J. Electron Spectrosc. Relat. Phenom.* 2018, 224, 27; F. D. Hardcastle, I. E. Wachs, *Solid State Ionics* 1991, 45, 201.
- [50] W. G. McMullan, J. C. Irwin, *Solid State Commun.* 1983, 45, 557.
- [51] M. S. Dresselhaus, A. Jorio, R. Saito, *Annu. Rev. Condens. Matter Phys.* 2010, 1, 89.
- [52] A. J. Owen, K. W. Sykes, D. J. D. Thomas, P. White, *Trans. Faraday Soc.* 1953, 49, 1198.
- [53] J. Halim, K. M. Cook, M. Naguib, P. Eklund, Y. Gogotsi, J. Rosen, M. W. Barsoum, *Applied Surface Science* 2016, 362, 406.
- [54] L. Najafi, S. Bellani, R. Oropesa-Nuñez, B. Martín-García, M. Prato, V. Mazánek, D. Debellis, S. Lauciello, R. Brescia, Z. Sofer, F. Bonaccorso, *J. Mater. Chem. A* 2019, 7, 25593.
- [55] K. Liang, S. Pakhira, Z. Yang, A. Nijamudheen, L. Ju, M. Wang, C. I. Aguirre-Velez, G. E. Sterbinsky, Y. Du, Z. Feng, J. L. Mendoza-Cortes, Y. Yang, *ACS Catal.* 2018, 9, 651.
- [56] S. Sun, H. Li, Z. J. Xu, *Joule* 2018, 2, 1024.
- [57] S. Brunauer, P. H. Emmett, E. Teller, *J. Am. Chem. Soc.* 1938, 60, 309.
- [58] J. Rouquerol, D. Avnir, C. W. Fairbridge, D. H. Everett, J. M. Haynes, N. Pernicone, J. D. F. Ramsay, K. S. W. Sing, K. K. Unger, *Pure Appl. Chem.* 1994, 66, 1739.
- [59] K. Liang, L. Guo, K. Marcus, S. Zhang, Z. Yang, D. E. Perea, L. Zhou, Y. Du, Y. Yang, *ACS Catal.* 2017, 7, 8406.